Evaluation of Planetary Boundary Layer Parameterization Schemes Using WoFS Ensemble Members and Observations from TRACER

FRANCESCA LAPPIN,[a,d] TYLER BELL,[a] PETRA KLEIN,[a] JEREMY A. GIBBS,[c] AND KENT KNOPFMEIER[b,c]

[a] *University of Oklahoma, Norman, Oklahoma*
[b] *Cooperative Institute for Severe and High-Impact Weather Research and Operations, Norman, Oklahoma*
[c] *National Severe Storms Laboratory, Norman, Oklahoma*
[d] *German Aerospace Center (DLR), Oberpfaffenhofen, Germany*

(Manuscript received 5 May 2025, in final form 23 January 2026, accepted 6 February 2026)

ABSTRACT: Coastal breeze circulations [bay breeze (BB) and sea breeze (SB)] modulate weather conditions by advecting a maritime air mass onshore, altering air quality, and often initiating deep convection. Coastal breeze interactions with the planetary boundary layer (PBL) are not well simulated due to small-scale interactions being parameterized by numerical weather models. As part of the Tracking Aerosol Convection Interactions Experiment (TRACER) in Houston, Texas, PBL observations from remote sensors and uncrewed aerial systems provide a unique benchmark for evaluating model performance and investigating underlying processes. The Warn-on-Forecast System (WoFS) is a convection-allowing, 18-member ensemble designed to predict high-impact weather by combining rapidly updating data assimilation cycles with varying PBL and radiation parameterizations. The TRACER datasets are used to evaluate WoFS's simulation of the PBL, coastal breezes, and their interactions with high vertical and temporal resolution. There is broad variability across members in the depth, arrival time, and intensity of the simulated SB case. Moreover, only a subset of members simulate the preceding BB, but none do so accurately. The radiation scheme impacts the ability to simulate a BB and the onset time of the SB. The mixing scheme for PBL parameterization lends differences in depth, intensity, and evolution. Nonlocal mixing schemes allow baroclinic circulations to develop more readily, thus simulating coastal flows better, but overestimate PBL depth and temperature. The influence parameterization schemes have on meteorological biases offers potential solutions to improve simulations of coastal PBL processes.

KEYWORDS: Boundary layer; Sea breezes; Unpiloted aerial systems; Model evaluation/performance

1. Introduction

The planetary boundary layer (PBL) fluctuates on a temporal scale from seconds to hours and on a spatial scale of centimeters to kilometers (Stull 2012). As computational efficiency has improved, operational numerical weather prediction (NWP) models can decrease the grid resolution and increase resolved processes in the atmosphere. Nevertheless, subgrid processes in the PBL still rely on parameterizations of surface fluxes, mixing length, and turbulent exchanges as a function of atmospheric stability (Stensrud 2007). Large-eddy simulations (LESs) reduce numerical assumptions by resolving the largest energy-containing eddies of the turbulent kinetic energy spectrum, thus representing the PBL stability and mixing length more accurately (Stoll et al. 2020). Due to the computational expense of LES, they are not yet feasible for NWP. There are numerous PBL parameterization schemes available in NWP models that vary the turbulence closure and how they transfer heat and momentum across model levels. Turbulence closure describes the order in which the nonlinear terms in the turbulence budget are modeled. Local mixing schemes can only interact with the adjacent model level, leading to slower vertical transport of heat, moisture, and momentum. Nonlocal mixing schemes allow vertical transport across the mixing length, which is more computationally expensive, but provides a more accurate depiction of the PBL.

There have been many studies to evaluate the performance of PBL parameterization during severe weather (Cohen et al. 2015), air quality (Hu et al. 2010; Xie et al. 2012), and coastal processes (Zhong et al. 2007; Miao et al. 2009). To summarize these, nonlocal schemes overmix the PBL and are often too warm and dry at the surface (Challa et al. 2009; Hu et al. 2010; Xie et al. 2012; Potvin et al. 2020), and local schemes create PBLs that are too cool and moist with overestimated wind speeds (Hu et al. 2010; Coniglio et al. 2013; Gómez et al. 2016; Arrillaga et al. 2016). The most accurate PBL scheme is difficult to determine because biases can differ across variables and a parameterization scheme's performance can depend on weather phenomena.

Coastal areas are particularly difficult to simulate accurately with NWP models due to the various land–air interactions and regional circulations. The PBL in these areas is more dynamic than the homogeneity assumed in the development of the associated parameterizations. Coastal clouds also play a strong role in radiative feedback; meanwhile, cloud coverage and depth are poorly modeled, historically (Huang et al. 2013). The sea-breeze (SB) circulation is a key component of the coastal environment during the warm season under weak synoptic conditions. While the SB has been thoroughly investigated, its contribution to convection initiation (CI) and altering air quality remains deficient due to a lack of PBL observations and sufficient model resolution. As the SB often provides lifting to trigger CI, accurately

Corresponding author: Francesca Lappin, francesca.lappin@dlr.de

DOI: 10.1175/WAF-D-25-0090.1

simulating the depth, timing, and propagation speed is critical to thunderstorm forecasting (Azorin-Molina et al. 2015; Boyer et al. 2025). Improving air quality forecasts is particularly important in coastal urban centers, like Houston, Texas, where high ozone can cause respiratory problems (Ryerson et al. 2003). Ozone exceedance has been linked to the SB circulation due to recirculation with minimal destruction of ozone precursors and reduction in cloud coverage (Banta et al. 2005; Darby 2005; Chen et al. 2019; Li et al. 2020; Stanier et al. 2021). Additionally, the SB can trigger thunderstorm development, which can lead to ozone production (nitrogen fixation from lightning) and destruction (decreased insolation and ozone precursor scavenging) (Cuchiara et al. 2023). The complicated influence the SB circulation has on ozone makes it a critical component to simulate accurately in NWP models.

NWP models succeed in simulating SB occurrences, but accurate timing and intensity are not always well captured. Numerous studies have noted that the Weather Research and Forecasting (WRF) Model frequently delays SB onset (Miao et al. 2009; Salvador et al. 2016; Caicedo et al. 2019; Zhang et al. 2022). The time of SB passage with respect to the boundary layer regime (stable, convective, or transitioning) influences the strength of SB impacts on turbulence intensity and PBL state variables (Arrillaga et al. 2018). Arrillaga et al. (2020) further determined that the WRF Model performance of simulating temperature, moisture, and PBL depth varies with the PBL regime. Additional water bodies can induce their own breeze circulations (i.e., bay, lake, river) that alter the evolution of the SB (Baker et al. 2001; Lappin et al. 2025). In a WRF Model evaluation of the SB impacts on ozone around Houston, Caicedo et al. (2019) found that the model failed to simulate the Galveston Bay breeze (BB), leading to an underestimation of ozone levels around Galveston Bay.

A number of studies have reviewed the impact of PBL and land surface characteristics on the coastal environment and SB evolution. The PBL parameterization choice can alter the PBL depth, strength of the SB in terms of wind speed and temperature advection, and SB timing. Nonlocal schemes have the tendency to have lower biases for SB wind speed and temperature at the surface compared to local schemes (Arrillaga et al. 2016; Cana et al. 2020; He et al. 2022). Salvador et al. (2016) attributed differences in scheme performance of PBL depth and wind speeds to variations in land surface parameterizations, like surface soil temperature. Gómez et al. (2016) used radiosondes to gauge the representation of the thermodynamic structure and found there are strong differences in PBL moisture, temperature, and lapse rate between the local and nonlocal mixing schemes. This is in contrast with results from He et al. (2022), which show similar thermodynamic structure across PBL schemes. Previous studies have relied on surface observations and radiosonde data to represent the PBL, which undersample the surface layer and rapid changes to the stability profile. Zhang et al. (2022) and Salvador et al. (2016) utilized vertical wind profilers to investigate the horizontal wind biases with height but lacked thermodynamic profile data to understand stability impacts. A complete verification dataset with high-resolution thermodynamic and kinematic observations throughout the evolution of a coastal breeze is necessary to understand the coastal PBL interactions.

In this paper, we analyze the evolution from BB to SB from the Tracking Aerosol Convection Interactions Experiment (TRACER) campaign set in the Houston–Galveston area. This is done through an intercomparison of PBL data from uncrewed aerial systems (UASs) and remote sensing platforms to ensemble members from a rapidly updating, high-resolution model. Each model ensemble member has a different parameterization configuration, allowing us to identify discrepancies from physical assumptions. Analyzing how the SB is simulated across different model parameterizations is critical to understand how the SB influences CI and air quality forecasts. Small biases in the timing, depth, and intensity of the SB can cause large differences in PBL response. The PBL dataset from TRACER provides observations for model validation with high vertical resolution throughout the mixed layer.

2. Methods and data

TRACER was motivated to understand the convective cloud life cycle and its interplay with aerosols (Jensen et al. 2022). Observations of cloud characteristics, air composition, and atmospheric state were gathered from May to September 2022. Cloud life cycles often begin within the PBL and depend on low-level moisture, aerosol composition, and momentum. The juxtaposition of urban sprawl, heavy industry, and water bodies makes the Houston–Galveston region a unique urban–coastal boundary layer to sample and evaluate. For this study, PBL profiler data constitute the verification dataset, including remote sensing platforms and UAS. Figure 1 shows the data collection sites from TRACER used to evaluate the model performance. Each location had a thermodynamic and kinematic profiling unit, but not all data from the case were available. Most of the analysis comes from the University of Houston Coastal Center (UHCC), located near the Galveston Bay coastline, because it allowed the BB and SB to be observed by UAS and remote sensing platforms.

a. Data

A primary verification dataset comes from UAS observations due to the high vertical and temporal resolution. The CopterSonde3 is a vertically profiling UAS with shielded temperature and humidity sensors (Segales et al. 2020). Each CopterSonde's sensor package is calibrated in the Oklahoma Climatology Survey calibration chamber prior to being used. The 2D wind vector was derived using a linear estimation from the aircraft's roll, pitch, and yaw angling (Palomaki et al. 2017). With a 3.5 m s^{-1} ascent rate and sensor sampling frequency of 10 Hz, the vertical resolution was set to 5 m and maintained at least 16 observations to average at each point. Only the ascent data are used because the wind vector coefficients are calibrated for an ascending platform and to avoid rotor wash. Further description of the UAS dataset and data processing can be found in Lappin et al. (2024).

Remote sensing observations came from two similar systems, the Collaborative Lower-Atmospheric Mobile Profiling System (CLAMPS) and the Space Science and Engineering Center Portable Atmospheric Research Center (SPARC;

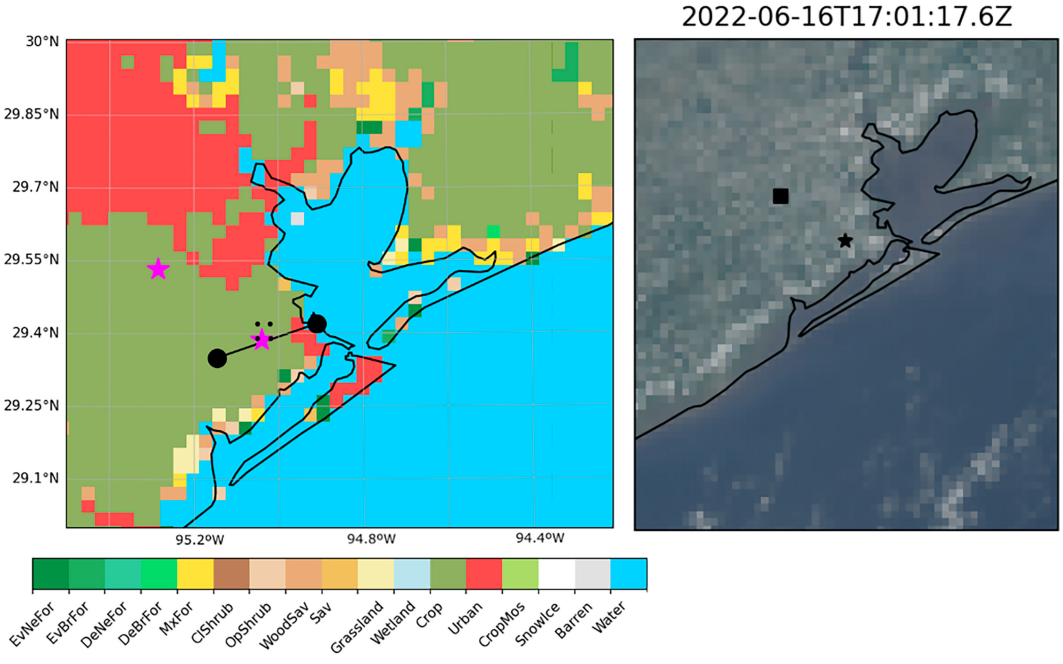

FIG. 1. (left) WoFS simulated land-use map with observation locations marked by pink stars. The black dots around UHCC indicate the four points averaged for bias statistics. The black line intersecting UHCC marks the cross-sectional line used in Fig. 15. (right) *GOES-16* satellite imagery at 1700 UTC 16 Jun 2022. The black star indicates the UHCC, and the black square marks the SPARC location. Land-use abbreviations are as follows: Ev = evergreen; Ne = needleleaf; For = forest; Br = broadleaf; De = deciduous; Mx = mixed; Cl = closed; Op = open; Sav = savannah; Mos = mosaic.

Wagner et al. 2019). Each was comprised of a scanning Doppler lidar and Atmospheric Emitted Radiance Interferometer (AERI). CLAMPS additionally had a microwave radiometer (MWR). The Doppler lidar operated a planned position indicator scan at 60° every 15 min, providing a vertical wind profile derived from the velocity azimuth display (Päschke et al. 2015); otherwise, the lidar was in a fixed-point vertical stare. The MWR and/or AERI data were processed with the Tropospheric Remotely Observed Profiling via Optimal Estimation (TROPoe; Turner and Blumberg 2019) to retrieve vertical temperature and moisture profiles every 10 min. The data processing procedures are uniform across the CLAMPS and SPARC observations. CLAMPS was located at UHCC, collocated with the CopterSonde, and was used to determine the PBL depth using TROPoe retrieval data. SPARC was located south of Pearland, Texas, 29 km northwest of UHCC. At SPARC, the effects of the SB were observed, but the BB was not detected since it is too far west from Galveston Bay. Unfortunately, excessive heat disabled the SPARC lidar during the afternoon (1815–2200 UTC).

The CopterSonde observations are the main verification dataset due to their high vertical and temporal resolution throughout the BB and SB. Observations from SPARC in Pearland, Texas, are used to evaluate the SB only and provide insight into how the simulated SB evolves as it penetrates inland.

b. Model

The Warn-on-Forecast System (WoFS; Stensrud et al. 2009; Heinselman et al. 2024) is a convection-allowing model with rapidly updating data assimilation cycles designed for high-impact weather events. The WoFS is initialized from the 36-member HRRR Data Assimilation System (HRRR-DAS; Dowell et al. 2022). The horizontal grid spacing is 3 km, and there are 51 vertical levels on a hybrid sigma–terrain-following coordinate system. The horizontal grid resolution is sufficient to resolve large water body (>200 km^2) breezes like the Galveston Bay breeze and the SB, based on previous works (Boybeyi and Raman 1992; Colby 2004). A finer-resolution simulation, like 1 km, would be necessary if the focus was to simulate the impacts from smaller water bodies (10–30 km^2) as determined in Hock et al. (2022). The vertical spacing is less than 100 m near the surface and expands up to 1 km at the 10-hPa model top; within the lowest 2 km, there are 12 vertical levels. For this analysis, the vertical spacing was standardized to 50 m within the lowest 2 km (i.e., 10, 60, … , 1960). Lateral boundary conditions are supplied by the operational HRRR forecast combined with large-scale perturbations from the GEFS (Zhou et al. 2022). Satellite, radar, and surface observations are assimilated every 15 min, with free forecasts generated every 30 min. The surface observations come from NCEP Prepared Binary Universal Form for Representation of Meteorological Data (PREPBUFR), assimilated with each cycle and daily satellite-derived sea surface temperature from the 0000 UTC NCEP Global Data Assimilation System (GDAS). The model is initialized at 1500 UTC, allowing 2 h of spinup and eight data assimilation cycles prior to the first forecast at 1700 UTC. For this study, the full forecast from 1700 to 2300 UTC is used with output every 10 min. There are 18 ensemble members (EMs)

TABLE 1. Parameterization combination (PBL and radiation) for EM1–EM6.

	Dudhia SW radiation	RRTMG SW radiation
YSU	EM01	EM02
MYJ	EM03	EM04
MYNN	EM05	EM06

varying in PBL and radiation parameterizations. Across all members, the microphysics and land surface schemes are fixed, using NSSL two-moment (Mansell et al. 2010) and the RUC (Smirnova et al. 2016) schemes, respectively. Beyond the initial and boundary conditions, the first six EMs vary only in shortwave (SW) radiation and PBL schemes and are the only members evaluated. The other members were examined and showed contrasts in behavior among PBL and radiation schemes that are similar to the first six and are excluded from analysis for space considerations.

Herein, we will focus on three PBL schemes frequently used in WRF modeling: MYJ (Janjić 1994) and MYNN (Nakanishi and Niino 2006) are both local mixing schemes with 1.5-order closure, and YSU is a nonlocal, first-order closure scheme (Hong et al. 2006). One main difference between MYJ and MYNN is how scaling relationships are derived; MYJ is based on observations, and MYNN is based on LES output. Each scheme varies in how the PBL depth is determined: YSU selects the lowest height at which a critical Richardson number, based on stability, is reached; MYJ is based on a turbulence kinetic energy (TKE) threshold where TKE < 0.1 m^2 s^{-2}; MYNN is similar to MYJ but requires the level to have a positive potential temperature (θ) gradient. Additionally, the effects of SW radiation schemes will be analyzed as members alternate between the Dudhia and RRTMG SW schemes. The Dudhia scheme is simpler and more efficient by not explicitly solving the radiative transfer equation but relies on empirically derived scaling equations and lookup tables (Dudhia 1989), whereas the RRTMG scheme is much more complex and computationally expensive, computing temperature tendencies throughout the profile and surface radiative fluxes by explicitly solving the radiative transfer equations (Iacono et al. 2008). Table 1 describes the parameterization combination for EMs 1–6.

While the WoFS model is primarily used for its probabilistic forecasts of severe weather, it also offers a way to evaluate model parameterizations with considerable realism, given extensive assimilated datasets. While the model is not geared toward PBL studies, it provides a benchmark to evaluate commonly used parameterizations for NWP to offer insight into best-performing combinations and potential improvements.

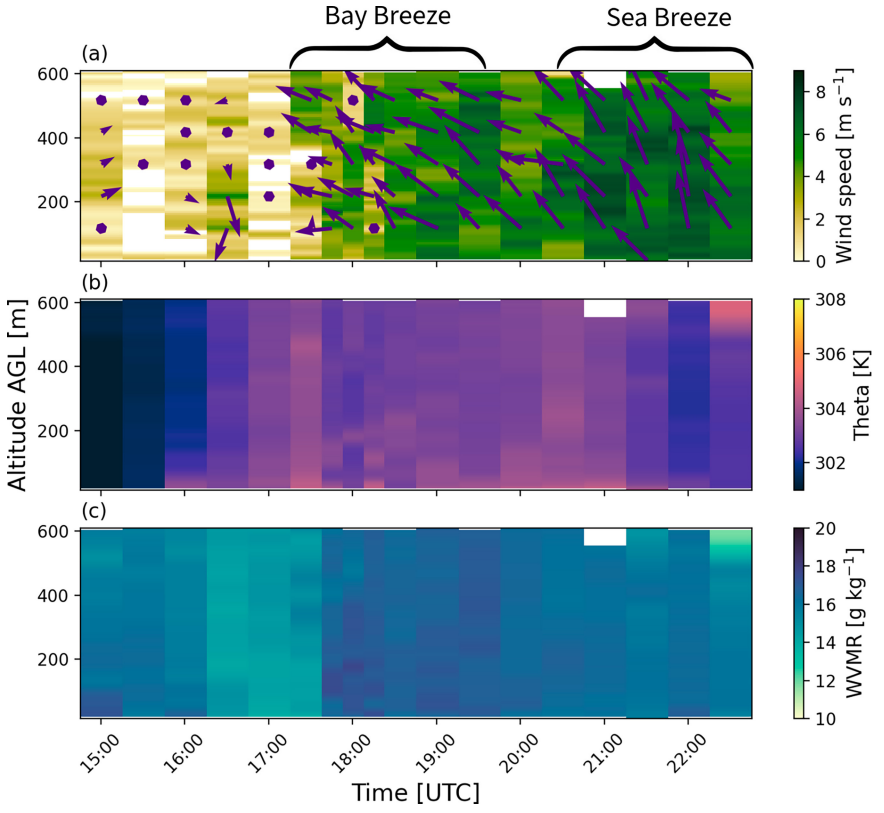

FIG. 2. (a) Wind speed (m s^{-1}) with direction arrows plotted, (b) potential temperature (K), and (c) WVMR (g kg^{-1}) observations from the CopterSonde at UHCC on 16 Jun 2022. Time in UTC (LST = UTC − 5).

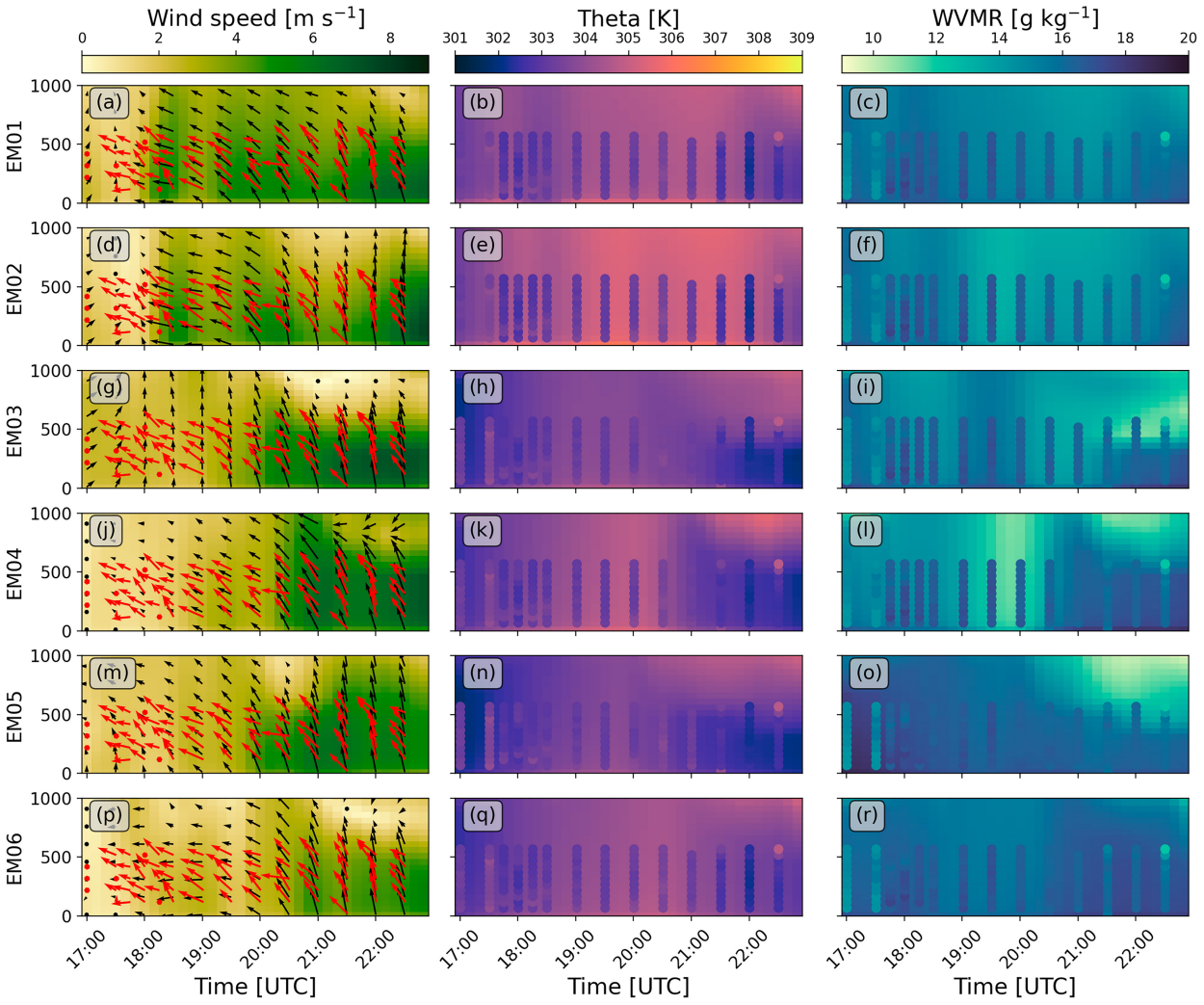

FIG. 3. (left) Shaded EM simulations of wind speed (m s^{-1}) with wind direction arrows (black) and observation arrows (red). (middle) Shaded EM simulations of potential temperature (K) with observation points overlaid. (right) Shaded EM simulations of WVMR (g kg^{-1}) with observation points overlaid. Each row represents a different EM.

c. *Case*

The 16 June 2022 event was chosen to investigate the interactions between the convective PBL and transition through BB and SB without the influence of precipitating convection (Fig. 2). Based on ASOS observations, the SB traveled from the coast [Angleton, Texas (KLBX)] to north of the Houston metro [Houston, Texas (KIAH)] from 1830 to 2300 UTC (not shown). Targeting a day with an observed BB is partially motivated by Caicedo et al. (2019) remarking on the importance of simulating the Galveston Bay breeze to local ozone forecasts. To isolate the interactions between coastal breezes and the PBL, a case with minimal interacting processes was preferred. During June 2022, coastal Texas was unseasonably hot and dry due to a strong midlevel high pressure system positioned over the southeast United States. At this time, the SB was common but rarely stimulated CI due to a lack of moisture beyond the PBL. Any successful convection was localized and short lived across the Houston–Galveston region. As a result, the BB and SB were uninterrupted by outflow boundaries, providing a clear look at the inland progression. The *GOES-16* satellite image at 1701 UTC shows the cumulus field developing over the region with clouds building along the coastline (Fig. 1).

On 16 June 2022, the CopterSonde completed 18 vertical profiles at UHCC. The UAS flew to 609 m at a cadence of 30 min, except from 1745 to 1830 UTC when the cadence was increased to 15 min. The observed BB traversed UHCC at 1730 UTC followed by clockwise rotation of the flow and acceleration of southeasterly winds at 2030 UTC, marking the SB passage (Fig. 2). Following the BB, moisture increased and potential temperature decreased throughout the profile. After the SB, cooling was more pronounced, while moisture advection was minimal.

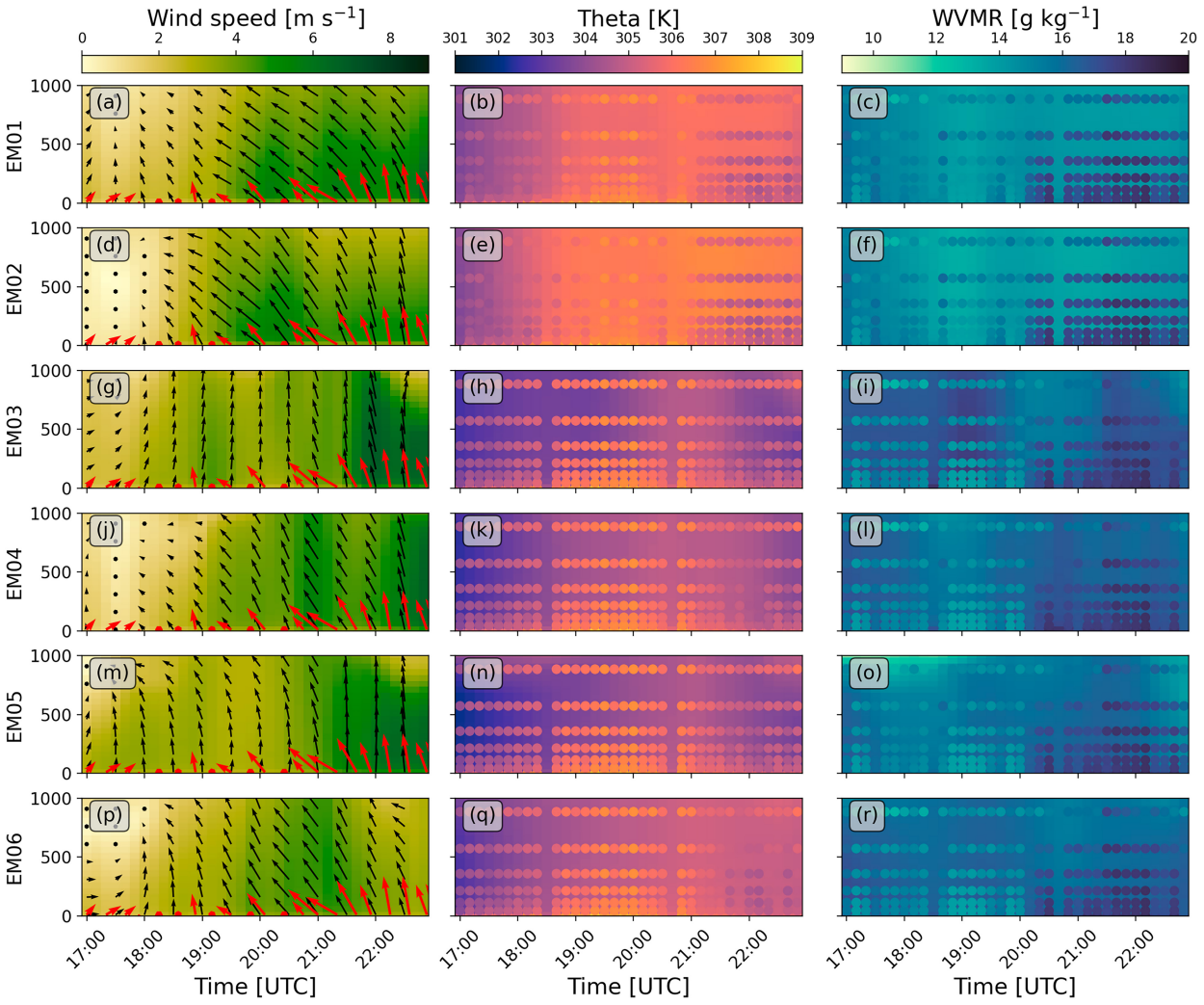

FIG. 4. As in Fig. 3, but model data are from the grid nearest SPARC and thermodynamic observations are TROPoe retrievals from SPARC. Red vectors are the 10-m surface observations from the Pearland Regional Airport ASOS.

d. Methods

1) SEA-BREEZE AND BAY-BREEZE IDENTIFICATION

At each location, the BB and SB were identified to determine the accuracy of timing and intensity. Pearland (SPARC) is too far from Galveston Bay to experience the BB. UHCC is located 15 km west of Galveston Bay, which provides a distinct wind direction shift from the BB versus the SB. Here, we define the BB as sustained winds greater than 2.5 m s^{-1} coming from 60° to 130° for at least 60 min. The SB is defined as winds greater than 3 m s^{-1} coming from 125° to 190° for at least 2 h. These thresholds were calculated from the average wind speed and direction after breeze passage using the CopterSonde dataset gathered at UHCC, throughout TRACER (Lappin et al. 2024). Specifically for June, these thresholds encompass the average surface wind speed increase after breeze passage determined in Wang et al. (2024). The detection is performed on the wind vector at the 110-m model level and averaged over the observed 609-m profile. The overlap in wind direction allows the BB to slowly transition to the SB without being penalized. The passage time is then marked as the first window that meets the minimum time criteria.

2) EVALUATION

Mean bias was chosen to evaluate the model performance against observations because relative bias overinflated values when wind speeds were near zero. First, the CopterSonde's 5-m resolution was linearly downsampled to 50 m to match the simulated vertical grid, and the forecast time was paired to the nearest flight time. A four-point nearest neighbor average was performed around each verification site, as seen in Fig. 1, and the mean bias compared to the CopterSonde was calculated. The bias data were subdivided into height layers and time spans. The height layer 20–200 m was chosen to represent the surface layer, while 200–400 and 400–600 m represent the mixed layer and, potentially, the

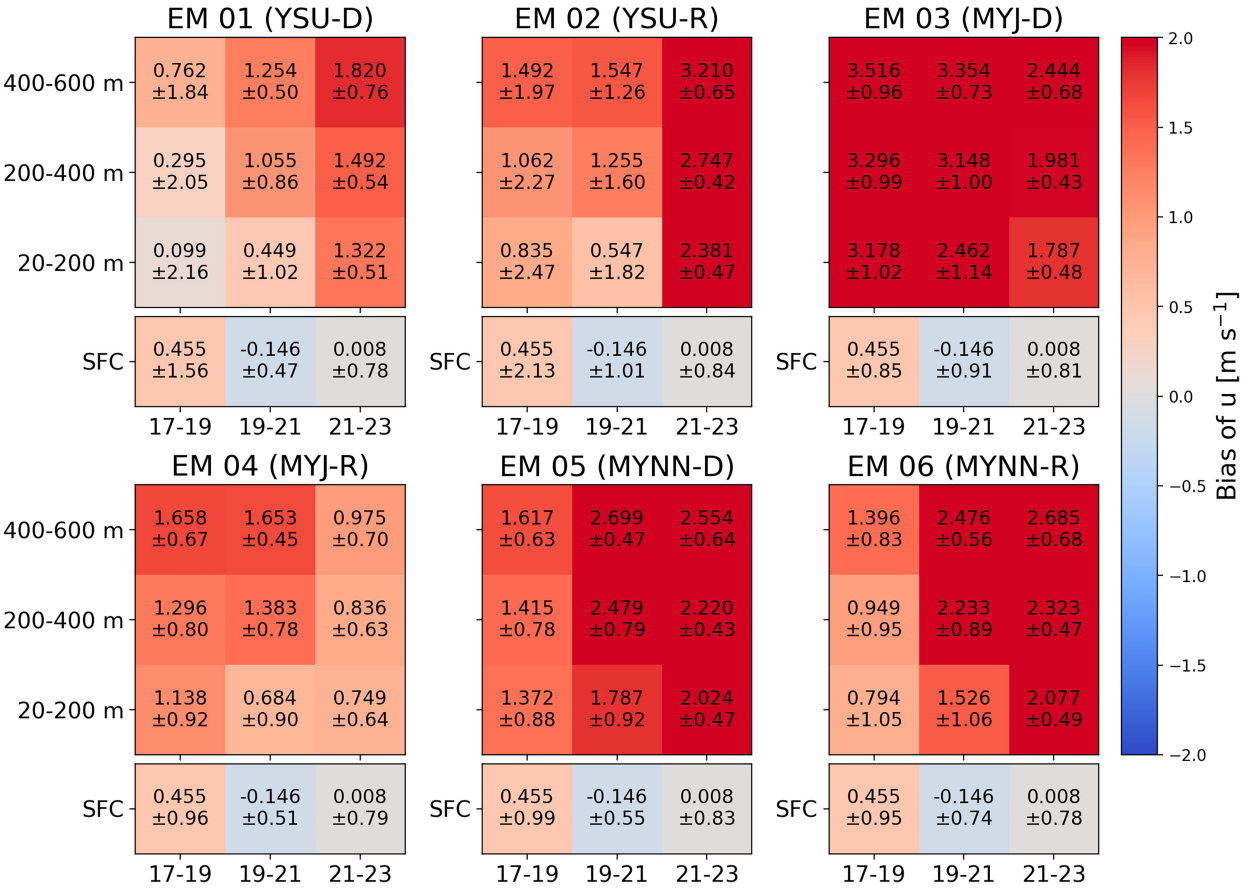

FIG. 5. Mean bias (model − observation) heat maps for each EM for the *U* component of the wind. Observations are from the CopterSonde at UHCC, and the model data are a four-point nearest neighbor to the UHCC average. The mean and standard deviation are in each text box. The time spans (columns) are in UTC, and height layers (rows) are in meters. SFC indicates data at 10 m.

top of the SB inflow layer. To understand how each breeze impacts the model performance, the forecast was divided into three categories: CBL/BB (1700–1900 UTC), transition (1900–2100 UTC), and SB (2100–2300 UTC). These time periods were selected to encompass the BB and SB timing for the first six EMs. The 10-m meteorological tower at UHCC was used for state variable observations compared to the 10-m model grid level.

3. Results

There are multiple components that must be accurately simulated to achieve a successful forecast, including the base environment, driving factors (i.e., the BB and SB), and the interactions between them. The analysis will follow with an overview of the environmental evolution for model and observations and a statistical evaluation of the PBL characteristics (section 3a). Then, the accuracy of the simulated BB and SB will be gauged in terms of timing, intensity, and depth (section 3b). A discussion on drivers of the BB will follow to explain the various ways the BB is simulated (section 3c).

a. PBL representation

Figure 3 shows the first six EMs' full forecast evolution of the lowest 1 km with CopterSonde observations overlaid for comparison. Most EMs evolve in the first 1–3 h as a typical growing CBL with moisture being mixed vertically as temperature increases under weak winds, similar to those conditions observed from 1500 to 1700 UTC (Fig. 2). As typical of local mixing schemes, EM04–EM06 warm more gradually throughout the day. There is considerable spread in the flow evolution throughout the BB onset and transition to the SB. The increase in easterly flow to 4–5 m s^{-1} indicates the BB in EM01 and EM02 (Figs. 3a,d). In EM04, the BB is weaker, only increasing the easterly flow to 3 m s^{-1} (Fig. 3j). EM03, EM05, and EM06 fail to simulate a BB before the SB (Figs. 3g,m,p); it appears EM06 tries to initiate the easterly push, but the flow is not sustained. In turn, the lack of a BB leads to missing moisture advection during the early afternoon amid the diurnal mixing out of morning, low-level moisture. Most members are drier than the observations, except for the MYNN members (EM05–EM06), whose early overestimation of moisture disguises the lack of moisture advection throughout the afternoon (Figs. 3o,r). The EMs are 1–4 K warmer prior to the SB

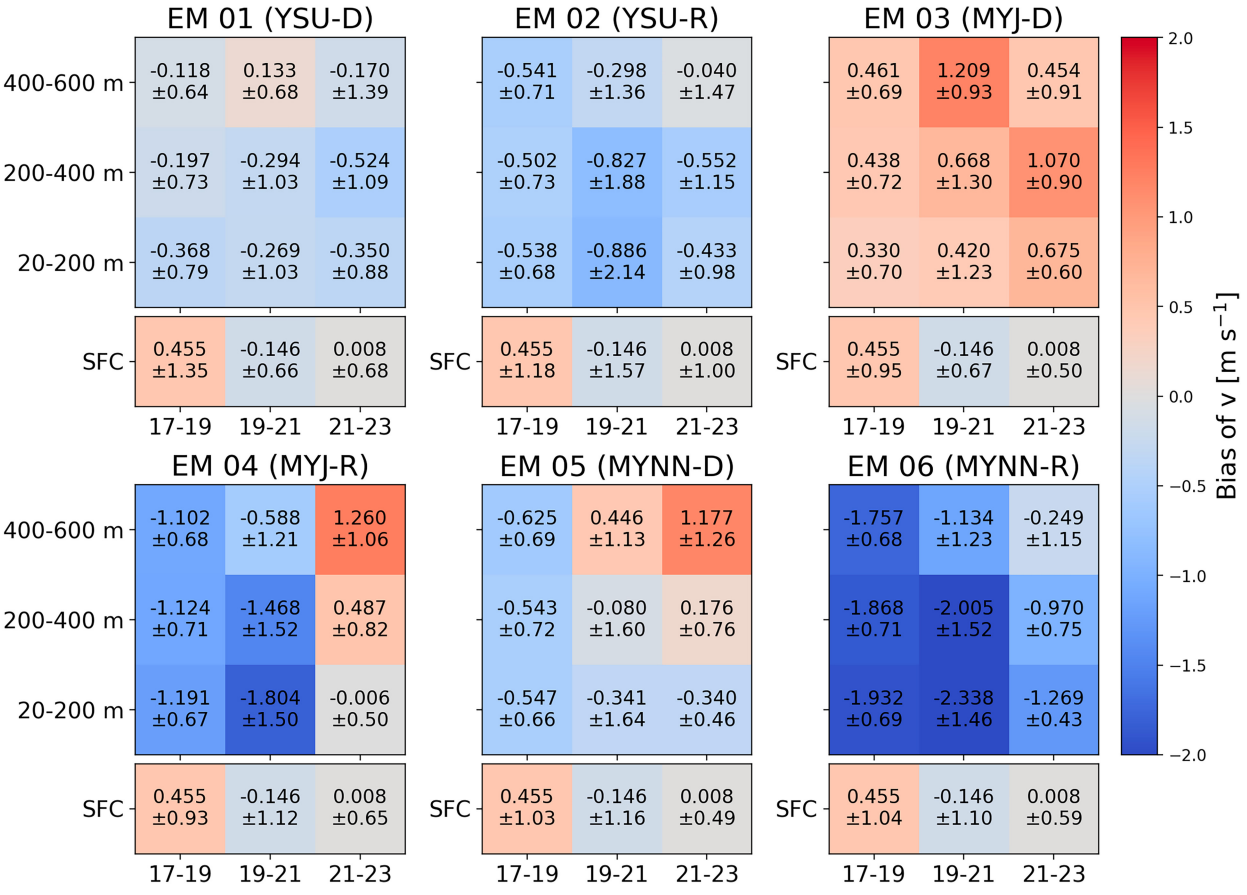

FIG. 6. As in Fig. 5, but for the *V* component of the wind.

and with much more diurnal variation than seen in the observations. The nonlocal mixing members (EM01–EM02) initialize the temperature most accurately but warm much more than observations (Figs. 3b,e); conversely, the local members (EM03–EM06) initialize too cool and take much longer to warm than observations (Figs. 3h,k,n,q). EM03–EM05 have the most distinct cool and moist SB inflow layers after 2100 UTC to varying depths (Figs. 3g–o). Some of these differences within the BB and SB can be related to the speed of onshore flow. The MYJ members show the fastest onshore flow with the most defined thermodynamic gradient between the SB inflow layer and residual flow aloft (Figs. 3m–r). Among the local members (EM03–EM06), the Dudhia members have the most distinct thermal internal boundary layers, marked by sharp shifts in temperature and moisture below 600 m (Figs. 3h,i,n,o). However, this does not align with the depth of onshore flow, which extends around 200 m higher in EM03 and EM05 (Figs. 3g,m).

Observations from SPARC can be used to compare the spatial heterogeneity of the simulated SB progression. SPARC was positioned in Pearland, Texas, further inland and away from Galveston Bay such that the region only experienced the SB passage around 2035 UTC. Unfortunately, a loss in Doppler lidar data collection from 1815 to 2200 UTC prevents looking at the onset of onshore flow, so the SB passage is estimated from a response in potential temperature, moisture, and ASOS surface wind observations. Unlike at UHCC, the early forecast hours show a weaker diffusion of low-level moisture and stronger flow, leading to a slower-developing CBL. The simulated SB onset is quite different compared to the evolution at UHCC (Figs. 3 and 4). While all members show some onshore flow after 1900 UTC, there is a wide variation in evolution and speed. However, there is not a substantial thermodynamic response until after 2100 UTC when some members (EM03–EM05) present onshore flow acceleration (Figs. 4g–o); meanwhile, the other members (EM01, EM02, EM06) have very little change in moisture or temperature throughout the forecast period (Figs. 4a–f,p–r). The potential temperature evolution across local and nonlocal PBL members is similar to UHCC's evolution, but the simulated temperatures tend to be lower than observations (Figs. 3 and 4). The MYJ members capture the moisture advection by the SB most accurately of all EMs but still underestimate the post-SB magnitude of low-level water vapor (Figs. 4p–r). Even in those members, the SB is simulated much deeper and lacks a clear boundary between the residual CBL air mass aloft, as seen at UHCC in EM03–EM05 (Figs. 4g–o). It is known that the depth of the SB increases as it moves inland (Garratt and Physick 1985; Melas and Kambezidis 1992), but in this case, it may be rising too quickly, leading to diluted SB

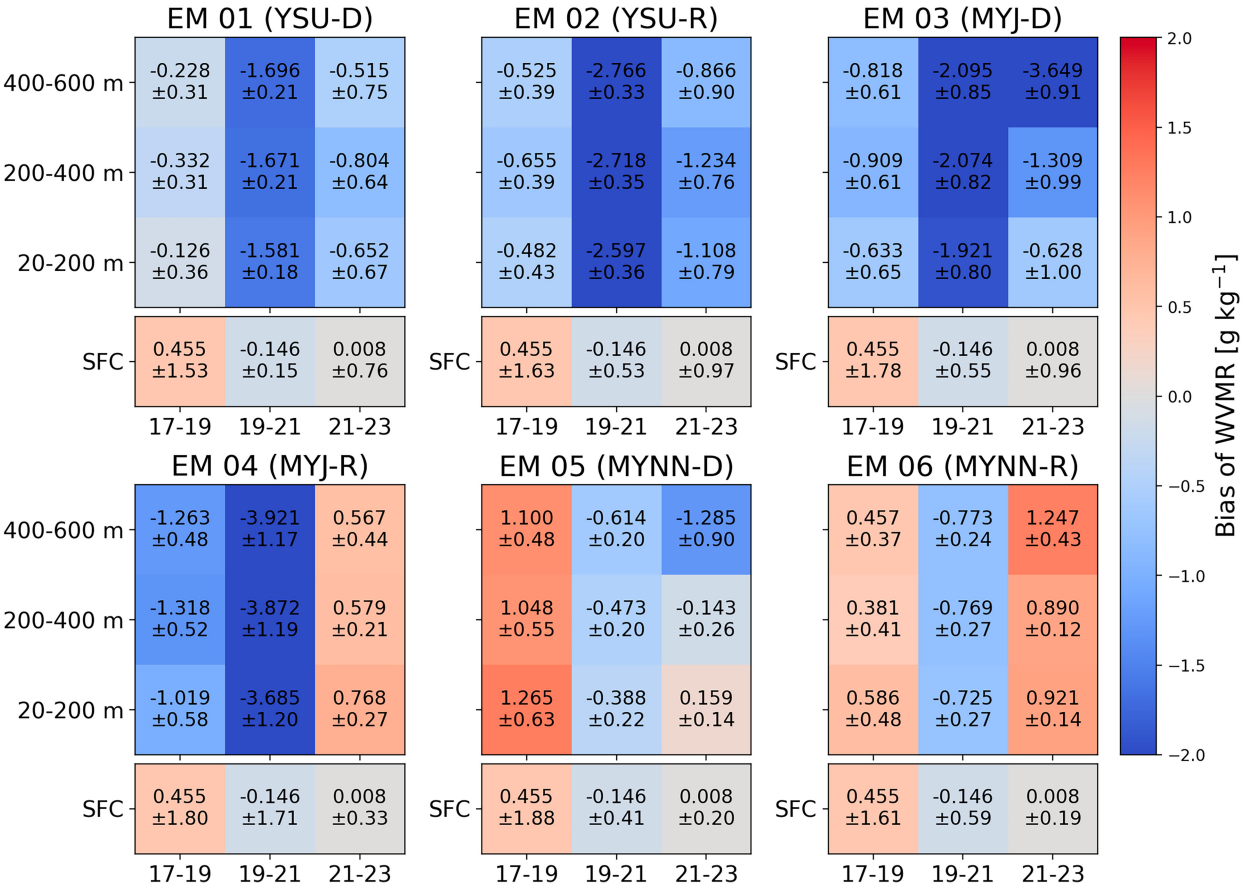

FIG. 7. As in Fig. 5, but for WVMR.

thermodynamic effects. While these are just two points, they show the difficulty in generalizing the biases across EMs with respect to time and variable of interest.

BIASES

In previous works, model biases have been calculated from surface observations and radiosonde observations, which can offer seasonal or regional differences. However, these datasets lack the resolution to understand the PBL-scale impact from mesoscale processes. It is important to measure how representative surface errors are to those within the mixed layer. The following analysis compares the EM mean biases across three height layers and three time spans to identify trends across members and forecast lead times. The lowest layer 20–200 m includes most of the surface layer and the transition to the mixed layer. The 200–400- and 400–600-m layers are typically in the mixed layer, but in some EMs, the top of the SB inflow layer dips below 600 m (Figs. 3i,l,o). Additionally, surface meteorological tower observations are included to see how the traditional verification method compares to biases above the surface. The time bins were selected to capture the CBL or BB passage time (1700–1900 UTC), the BB to SB transition (1900–2100 UTC), and the pure SB regime (2100–2300 UTC). To keep the verification consistent with in situ measurements, only the CopterSonde observations are used above the surface.

Since EM03, EM05, and EM06 failed to produce a BB, these EMs have the largest zonal wind bias above the surface (Figs. 3g,m,p, and 5). The zonal bias magnitude tends to increase with height and throughout the afternoon. The errors in the surface and mixed layer are often much more significant than what is observed at 10 m, but the standard deviations are similar (Fig. 5). With parameterizations commonly refined using surface observations, adjustments based on surface errors could cause adverse effects in the mixed layer. If only the surface observations were used, it would appear that the model simulates the zonal wind much better than when the whole PBL was considered. Meridional wind biases are generally lesser in magnitude than zonal wind biases and peak in the BB–SB transition period (1900–2100 UTC) caused by inaccuracies in SB onset time (Fig. 6). There is also much less consistency in bias trends with height across members and time spans. Most EMs underestimate the wind speeds, especially the zonal component, leading to more southerly SBs than the observed south-southeasterly conditions (Fig. 3). This is interesting due to the coastal geometry of the site; directly

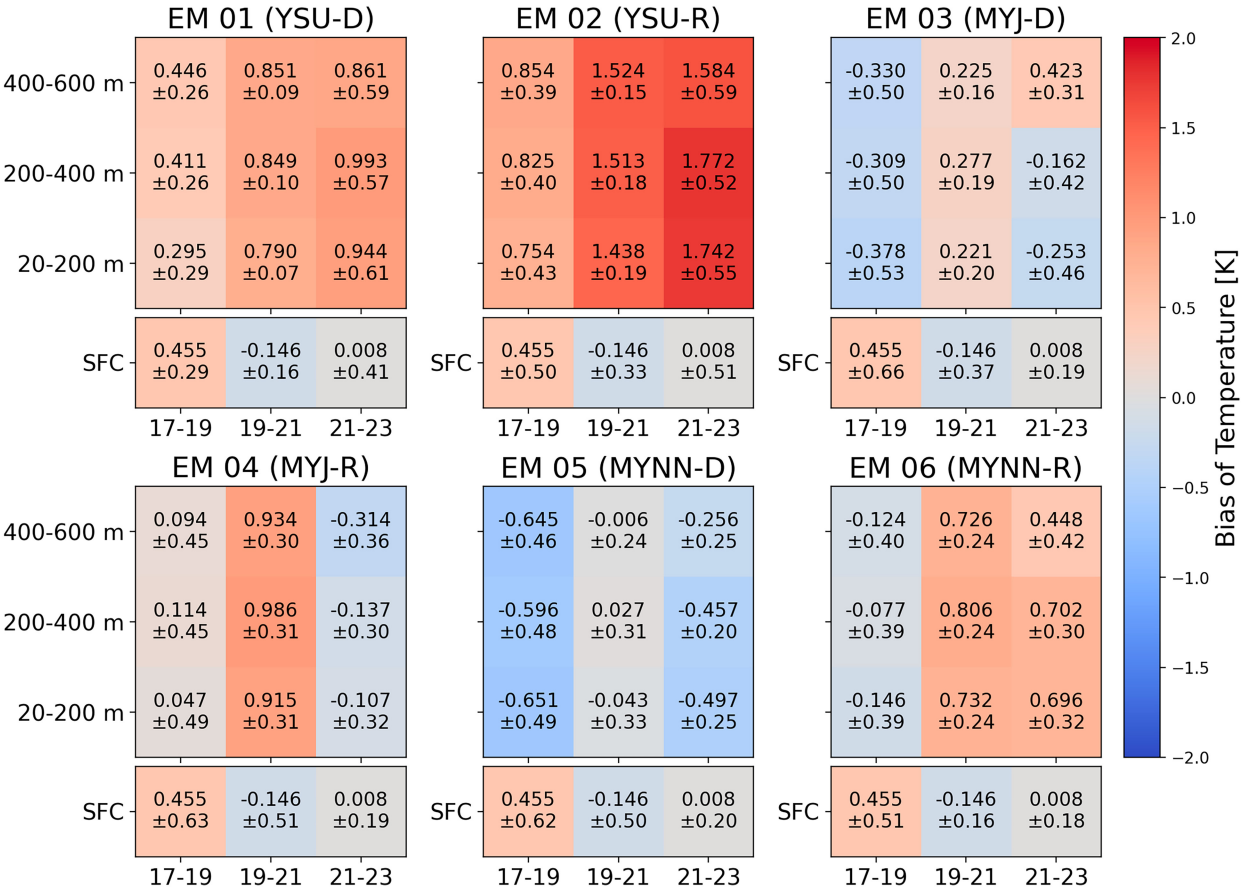

FIG. 8. As in Fig. 5, but for temperature.

onshore flow falls near 135°, and purely southerly flow has more land to traverse than if the flow were truly shore perpendicular.

Similar to the meridional wind, the largest moisture biases exist in the SB transition time span from 1900 to 2100 UTC, as the moisture advection gradually strengthens (Fig. 7). Moisture biases are more uniform across the height layers for each period, but the difference in biases between the surface and mixed layers can be sizable, especially for MYNN members (EM05–EM06). Water vapor mixing ratio (WVMR) is mostly underestimated after the SB passage (Fig. 7). However, EM04 and EM06 overestimate the water vapor within the SB inflow regime (2100–2300 UTC) as they have the shallowest thermal internal boundary layer (Figs. 3l,r). EM05 has the lowest magnitude of moisture bias, but that is due to the initial high moisture bias that equilibrates after the BB advects additional moisture, rather than an accurate representation of the thermodynamic evolution (Fig. 7). The differences in temperature bias are clearly divided by type of PBL mixing, with the nonlocal mixing schemes increasing with error throughout the day as the PBL is overmixed (Fig. 8), whereas the local schemes heat the PBL more slowly to begin with and then respond gradually to the changes induced by the SB, with the largest underestimation in the 2100–2300 UTC time frame. EM06 is a bit of an anomaly from this pattern because the SB is the weakest of all EMs in terms of wind speed, leading to underestimated cool-air advection (Figs. 3 and 8).

How each scheme represents various processes in the PBL can lead to performance varying with the variable. For example, the YSU scheme EMs tend to perform better in the kinematic representation of the PBL and upon initialization for the thermodynamics but quickly become too warm and overly mixed. The local mixing EMs have a lot of similarities in the temperature bias evolution but are sensitive to variations in the SB representation. This may lead to a collapse in model spread on local members, leading to slower-developing PBLs with poorer flow representation.

b. *Breeze characteristics*

As stated previously, most NWP models will successfully signal the occurrence of the SB when synoptic conditions allow. However, the details of simulated SB are often incorrectly represented, particularly with depth and time of arrival. The depth of the PBL is historically poorly simulated and dependent on PBL parameterization (Hu et al. 2010; LeMone et al. 2013). There is also broad variability in observed PBL depth based on the method, especially in the summer (Seidel et al. 2010;

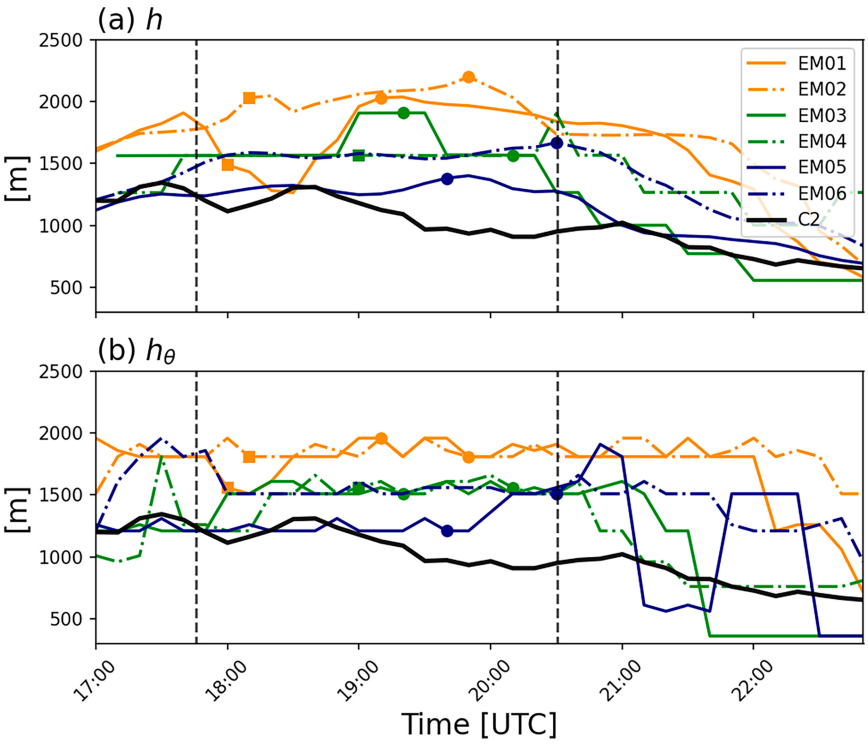

FIG. 9. PBL depth (a) native scheme method and (b) potential temperature gradient method for each member. CLAMPS2 observations determined PBL depth (thick black line; labeled C2 in legend). Squares indicate BB passage, and circles indicate SB passage. Vertical dashed lines indicate the BB (left) and SB (right) determined from the CopterSonde observations.

Sawyer and Li 2013). Furthermore, the depth of the SB inflow layer adds another important mixing length that can be viewed from a thermodynamic and kinematic perspective. These make finding a meaningful PBL depth complicated and alter the evolution throughout the afternoon and evening transition. The method to determine the PBL depth is specific to the PBL parameterization, which can elicit large differences in its estimation. To standardize the PBL depth detection method, the maximum potential temperature gradient method (Stull 2012) will also be applied to all EMs and observations. The scheme-specific PBL depth h and potential temperature gradient PBL depth h_θ are both shown in Fig. 9. It is also common to use h_θ to determine the depth of thermal internal boundary layers, which provides an estimate of the SB depth (Garratt and Physick 1985).

Both h and h_θ have similar spreads across EMs through the forecast period (Fig. 9). The two detection methods vary most significantly for EM01, EM02, and EM05. For YSU EMs, h_θ is more consistent throughout the afternoon and begins to decay far later than h or any other EM h_θ. The agreement between h and h_θ is very similar until the SB passage. Interestingly, most members estimate the PBL deeper using the potential temperature gradient method, except for the MYJ members. This is because the YSU and MYNN schemes give weight to the potential temperature gradient when determining h, but MYJ uses a TKE method, which could be inflated by the shear driven at the top of the SB. For MYNN members, h is more steady and realistic than h_θ since the mixing lengths account for stability changes, allowing adjustments shortly after initialization and after the SB passage. Overall, h_θ performs worse after the SB due to a gradual transition in the thermodynamic profile.

Upon initialization, EM04–EM06 have an accurate estimate of h, compared to observations, but without the implications of the BB, these members grow the PBL too rapidly, leading to overestimates in depth. All members tend to overestimate h and h_θ to varying degrees. The YSU members overestimate h the most with 50%–120% relative bias; however, they are the only members to represent the brief h reduction after the BB. After each simulated SB, h begins to decay, while h_θ decays much later and more quickly. The rate of decay for h is much more realistic than the sudden decline in h_θ, and the h methods produce a more realistic evolution, especially after the SB and into the afternoon transition.

The SB passage timing follows similar complications, since inaccurate heating rates over land and water can cause SB onset errors on the order of hours. Time of day not only impacts the state of the PBL but also influences the strength of the SB in terms of wind speed and thermodynamic changes (Arrillaga et al. 2018). All members, except EM06, simulate the SB earlier than observed by 30–70 min (Fig. 9). Conversely, NWP models often predict the SB 1–4 h later than observed in

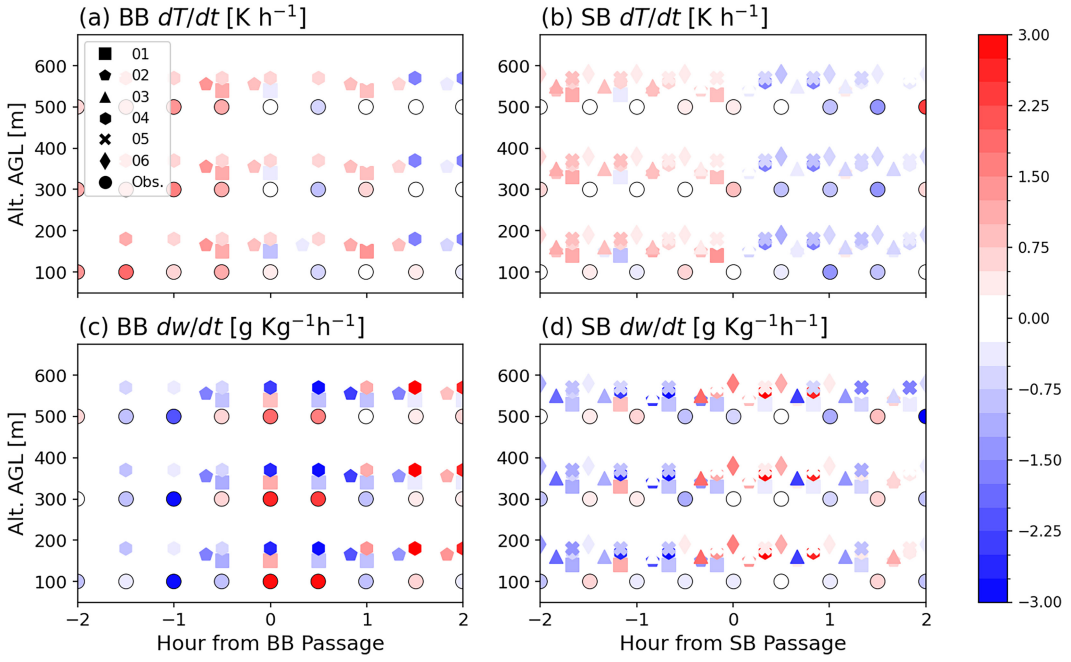

FIG. 10. Rate of change for temperature (K h^{-1}) by the (a) BB and (b) SB and rate of change of WVMR (g kg^{-1} h^{-1}) by the (c) BB and (d) SB. Only the three EMs that simulated the BB are plotted in (a) and (c). All EM rate of change values are calculated at the same height intervals.

Caicedo et al. (2019), which employed YSU and RRTMG. It must also be noted that the resolution of the observed SB frontal passage time is limited to a 30-min resolution, so the SB could have passed UHCC up to 20 min earlier than when it was sampled. In comparison, the timing in this work is simulated fairly well, possibly improved from the surface data assimilated upon initialization. For this event, the observed SB moved through during the CBL afternoon transition. Because all members simulated the SB too early, the CBL structure remains consistent between observations and simulations. If the SB had passed later than observed, it would have been during the afternoon–evening transition and likely would have inflated errors in potential temperature and moisture, as found in Arrillaga et al. (2020). The RRTMG members have more accurate SB passage timing compared to Dudhia members. The RRTMG members better depict the radiative transfer through moist air (Montornès Torrecillas 2017), allowing the circulation to develop more slowly than the Dudhia members.

Up until now, the thermodynamic evaluation has focused on the PBL with influences from the BB and SB. However, the accuracy of simulating the breeze intensity is equally important. Even small errors in the magnitude of moisture and temperature advection can greatly impact the preconvective environment. Figure 10 shows the rate of change for temperature (dT/dt) and water vapor mixing ratio (dq/dt) as a function of the BB and SB passages. The rate of change is calculated using a forward time difference and is standardized to 30-min intervals; for more information, see Lappin et al. (2025). Prior to the BB passage, the members are in good agreement with the observation for the diurnal warming and drying of the early afternoon PBL (Figs. 10a,c). After the BB, the magnitude of cooling and moistening is underestimated by all members for 1.5 h. EM01 has the best representation of slight cooling at BB passage, but it transitions to a warming trend after 1 h, where the observations show near-zero temperature change for 2 h after the BB (Fig. 10a). The moisture response for EM01 is even shorter lived but is still the most representative of the observed environment (Fig. 10c). The other members (EM02 and EM04) show an enhanced drying response within the BB, indicating the BB has very little impact on simulated convective mixing.

There are some similarities with the SB response, with better agreement prior to the SB passage and increased spread in moisture advection after the SB passage. Without thermodynamic influence from the BB, most members have warming and drying rates that are stronger than observed (Figs. 10b,d). The error magnitude for the SB dT/dt is small, as are the overall cooling rates. Meanwhile, the dq/dt errors show overestimation after the SB (Fig. 10d). Some members (EM02, EM04, and EM06) forecast strong moisture advection with the SB, that is not observed due to the influence of the BB. EM05 has the smallest overall difference for dT/dt and dq/dt after the SB passage, even though it lacks a simulated BB. To some extent, simulating the BB is not necessary to accurately represent the SB; however, slowing the CBL growth is important for cooling potential, as seen in observations from Lappin et al. (2025).

c. *Bay breeze*

As previously mentioned, only half of the ensemble members simulate a BB that was observed to pass through the

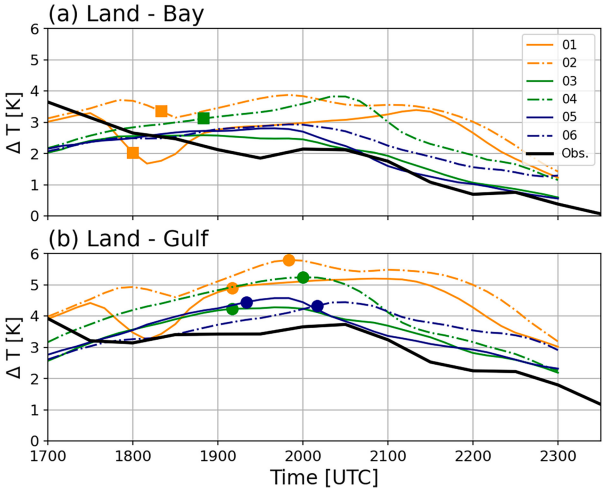

FIG. 11. (a) Modeled and observed (black line) difference in 10-m air temperature (K) between four-point nearest neighbor average at UHCC (29.39°N, 95.04°W) and grid point over Galveston Bay (29.45°N, 94.81°W). (b) 10-m temperature gradient (K) between four-point nearest neighbor average at UHCC and grid point over the Gulf of Mexico (29.08°N, 94.75°W). Squares represent the time of BB passage, and circles represent the time of SB passage.

UHCC site at 1730 UTC, and there are some obvious differences in the way the BB is simulated across the PBL schemes. The YSU scheme members have the earliest, most intense BB with a gradual weakening in the wind speeds as it transitions to the SB (Figs. 3a,d) and have the only noticeable moistening response to the increasing easterly flow (Fig. 3). EM04 is the only other EM to simulate the BB, but its onset is more gradual, occurs later, and has no thermodynamic reaction (Figs. 3j–l). EM06 has a brief period of easterlies around 1845 UTC, but it is too short lived to meet the criteria of a BB. Overall, EM01 has the best thermodynamic response to the BB of all the members, with stronger cooling and moistening than EM02 (Fig. 10). To improve future simulations of the BB near the coast, we look at the forcing behind the BB to identify where parameterizations diverge.

The BB circulation is induced by the surface temperature gradient across Galveston Bay but is weaker and does not propagate as far inland as the SB. Figure 11 shows the land–water gradient across Galveston Bay is 1–2 K less than the gradient across the Gulf of Mexico, but the separation across the members is similar. Most EMs overestimate the temperature gradient compared to observations, but the local PBL–Dudhia (EM03, EM05) EMs tend to perform the best. The YSU members have the largest land–water temperature contrast early on, correlating with the largest sensible heat flux H over land, similar to scaling relations from Crosman and Horel (2010). The BB induces a reduction in H and temperature gradients due to the clouds pushed inland, which is more drastic for EM01 due to the simpler cloud representation (Figs. 11 and 12). The land–bay temperature gradient for EM04 increases slightly more than the other local EMs due to minimal cloud cover (Fig. 12). The differences across EM temperature gradients are 0–2 K, with the most spread after the SB due to different cooling rates.

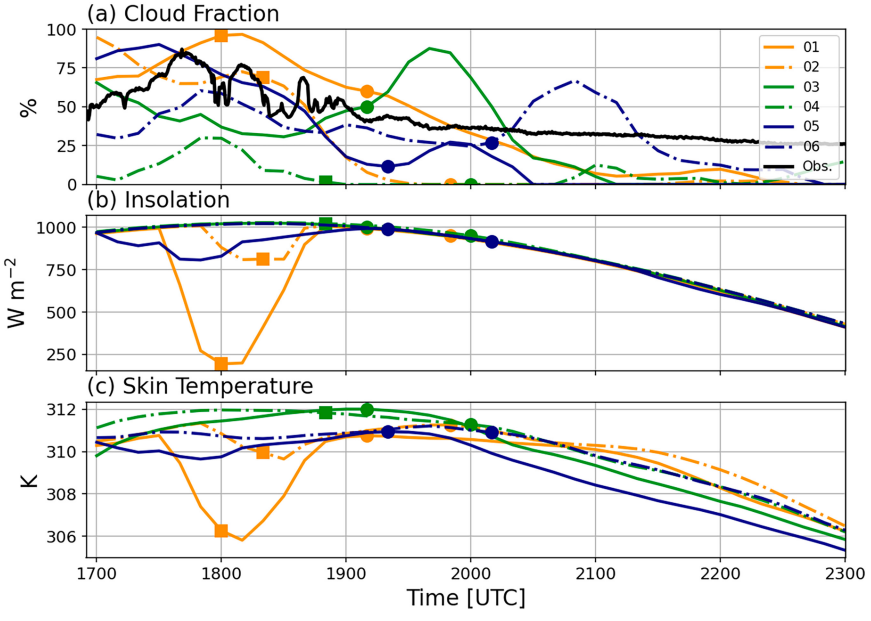

FIG. 12. Time series from each EM of (a) low-level cloud fraction (%), (b) incoming SW radiation (W m^{-2}), and (c) skin temperature (K). Computed as a four-point nearest neighbor average closest to the UHCC site. Squares represent the time of BB passage, and circles represent the time of SB passage. The black line in (a) is the cloud fraction from the total sky imager at the La Porte, Texas, AMF facility.

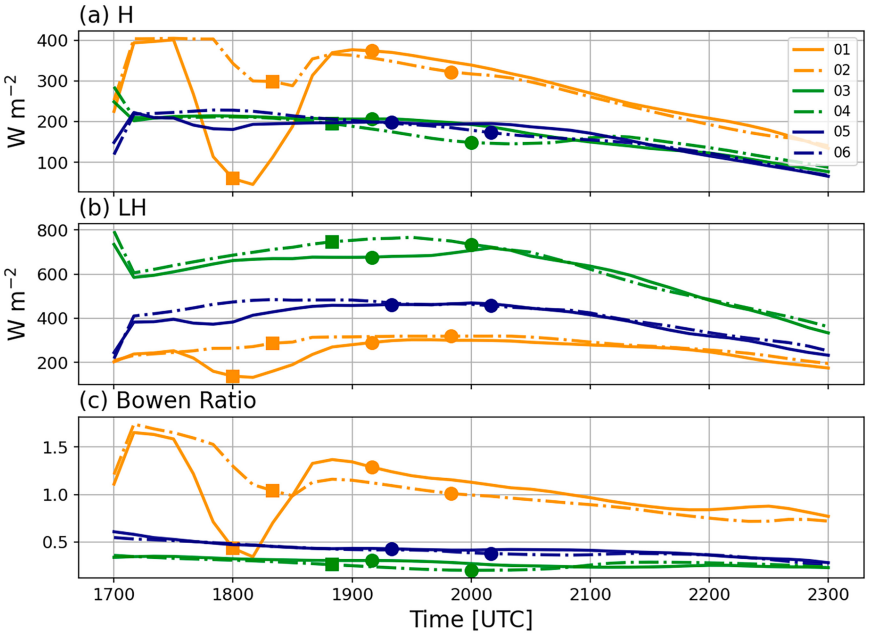

FIG. 13. Time series from each EM of (a) sensible heat flux (W m^{-2}), (b) LH flux (W m^{-2}), and (c) Bowen ratio (unitless). Computed as a four-point nearest neighbor average closest to the UHCC site. Squares represent the time of BB passage, and circles represent the time of SB passage.

The surface heat fluxes have similar distinctions from local and nonlocal EMs. The local EMs have similar magnitudes of H that evolve gradually, whereas the YSU EMs produce larger H that is more sensitive to changes in cloud cover. After the SB, H declines for all members and the spread collapses across the MYNN and MYJ members (EM03–EM06). Similarly, this is true for latent heat (LH) flux, but the magnitude of LH is very dependent on the PBL scheme (Fig. 13a). The MYJ EMs have markedly higher LH and comparable H to MYNN, which is atypical in previous climatologies (Shin and Hong 2011; Milovac et al. 2016). The Bowen ratio evolution is more steady than H or LH, aside from the drastic reduction due to clouds in the YSU EMs (Fig. 13c).

The SW radiation scheme also influences surface fluxes. This is most obvious when there are broken clouds and radiative processes are most complex. Figure 12a shows the most cloud variability exists in the morning, with a general decrease through the afternoon. Figure 14 shows the regional cloud fraction variability at 1700 UTC, and the degree of cloud cover and density varies across all EMs. After the SB, cloud cover briefly increases and then declines to near zero (Fig. 12a). This is also seen in observations from La Porte after 1900 UTC. As compared with RRTMG, Dudhia EMs tend to have higher cloud fractions, leading to less insolation reaching the surface and lower skin temperature (Fig. 12). While RRTMG EMs like EM04 and EM06 have more widespread cloud cover, the density of cloud coverage is less than that of EM03 and EM05 (Fig. 14). In comparison with the 1700 UTC satellite imagery in Fig. 1, the RRTMG EMs simulate the cloud fraction better in terms of magnitude and coverage. The relationship between cloud simulation and surface temperature is especially impactful on the nonlocal (YSU) EMs, as surface temperature is most sensitive to incoming SW radiation (Jia et al. 2023). Meanwhile, the surface temperature of the local PBL schemes (EM03–EM06) is more persistent prior to the SB, because it is sensitive to H, which is steady throughout the early afternoon (Figs. 12c and 13a).

Additionally, the local PBL schemes (EM03–EM06) simulate the skin temperature over the urban land use as much warmer than the nonlocal EMs, but across croplands near the coast, the difference is not as large (Fig. 14). It is possible that this large temperature gradient is causing the SB to overtake the BB circulation more often in the local schemes. This would align with the tendency for the simulated SB to arrive earlier than observed at both UHCC and SPARC (Figs. 4 and 9).

The first 3 h of the forecast has the most variability at UHCC, so the next analysis focuses on the 1730–1930 UTC period to capture the time the BB forms and passes through the region. Multiple factors impact coastal breeze inland propagation, such as H, PBL turbulence, and temperature gradients. To evaluate the BB environment, a transect from the Galveston Bay coastline across the UHCC and further inland (Fig. 1) was selected to determine the penetration distance of the BB and variability of driving forces. The fields were averaged from 1730 to 1930 UTC to capture consistent patterns. Herein, a BB is defined having a minimum wind speed of 2.5 m s^{-1} sustained for 1 h with wind direction from the bay coastline (60°–130°). Figure 15a designates the span of zonal wind that meets the criteria shaded in gray, and once the zonal wind speed is below that threshold, then the BB has ended its propagation inland. The BB in EM01 and EM02 travels the furthest inland,

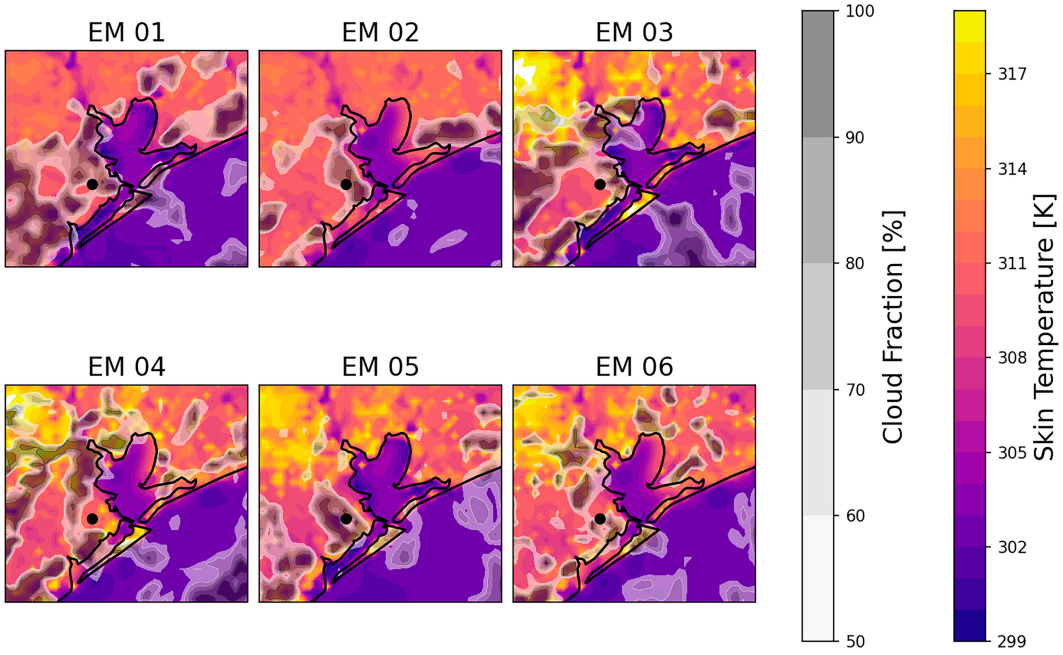

FIG. 14. Simulated skin temperature (K) with gray-filled contours of cloud coverage (%) for each EM at 1700 UTC.

between 13 and 15 km, while in EM03 and EM05, the BB penetrates the least distance and does not reach UHCC. The BB in EM04 and EM06 travels about the same distance inland, but the BB flow did not last long enough at UHCC to meet the criteria.

The drivers of the BB are divided by the type of PBL mixing scheme. Nonlocal mixing scheme EMs are more successful at producing a BB that reaches UHCC than local EMs. The YSU members have preferential BB development due to faster vertical transport of heat to generate baroclinicity. For these EMs, the land–water temperature gradient at 10 m is initially the largest, even though the skin temperature gradient is the lowest (Figs. 11 and 15). YSU EMs have the largest heat transfer coefficient, leading to a well-mixed surface layer and warm air over land (not shown). This allows the BB circulation to develop quickly, even with more cloud coverage over land (Fig. 12). The local schemes are more sensitive to cloud cover because they require a higher initial surface temperature to induce a BB. Initially, EM03 and EM05 have the highest cloud fractions over UHCC, among local EMs, leading to marginally lower surface temperatures than their RRTMG counterparts (Figs. 12a,c). As a result, the land–bay temperature gradient builds slowly and is not sufficient to force the BB as far inland as UHCC. EM06 is interesting because it appears to reach UHCC in Fig. 15a but does not meet the BB criteria. As compared with EM06, EM04 has faster zonal winds closer to shore that provide the BB with more inertia to reach UHCC. Across all members (EM01–EM18), these patterns follow, with 83% of YSU EMs simulating a BB, while MYJ and MYNN do so at 66% and 33%, respectively. While the MYJ and MYNN schemes are overall very similar, MYNN EMs have lower surface temperatures over land and weaker land–water temperature gradients (Figs. 11 and 15d).

4. Conclusions

Coastal breezes around the Houston area have a large impact on weather and air quality forecasts. The interactions between the PBL and coastal breezes occur on rapid time scales and induce vertical gradients that impact pollutant trapping and convection initiation. For these reasons, it is important to simulate such processes accurately in NWP models. This study examines how various PBL and SW radiation parameterizations impact the forecast skill of the BB, SB, and the implications on PBL evolution. By using a dataset of TRACER observations from PBL profilers, verification of model simulations can occur at a finer temporal and vertical resolution than is typically feasible. For this reason, a case study was evaluated in depth to understand the range of biases that may exist in time and space during complex coastal PBL transitions. The WoFS EMs were utilized to understand the impacts of parameterization combinations with improved realism from diverse data assimilation.

Observations from UAS have high vertical resolution (5 m) up to 609 m every 30 min, while observations from remote sensing platforms extend higher and are collected every 10 min. These observations allow the model to be evaluated on temporal scales consistent with the PBL evolution during coastal breeze passages. Previous studies have used long-term datasets to evaluate the surface representation and supplement the vertical profile with infrequent radiosondes. This work serves as a complement to provide a more resolved understanding of parameterization differences under rapidly changing conditions. It was found that many of the state variable mean biases

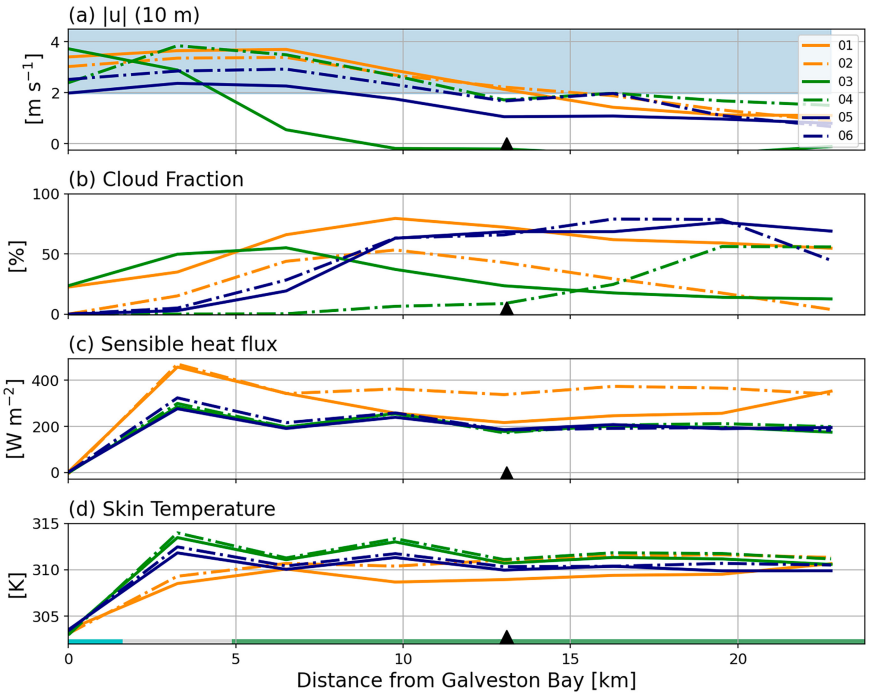

FIG. 15. Simulated transect from the Galveston Bay shoreline averaged from 1730 to 1930 UTC. The gray shading in (a) indicates the threshold for BB onshore flow. The black carat indicates the point in the cross section where UHCC lies. The bars at the bottom of (d) indicate the land use throughout the cross section with blue—water, gray—urban, and green—croplands. (a) The absolute value of the zonal wind component (m s^{-1}), (b) the cloud fraction (%), (c) the sensible heat flux (W m^{-2}), and (d) the skin temperature (K).

can differ in sign and magnitude from the surface to the mixed layer, particularly the wind vector (Figs. 5–8). While the SB is fairly well represented in timing and magnitude, the BB is often too weak to propagate as far inland as observed (Fig. 3). Because the BB circulation is more weakly forced, it is sensitive to surface temperature over land and the rate of vertical heat transport. For this reason, the nonlocal mixing PBL scheme (YSU) had more success at simulating the BB than did local schemes. Similar to Cana et al. (2020) and Salvador et al. (2016), YSU performs better kinematically. The radiation scheme also plays a large role in BB formation in local schemes. For instance, Dudhia EMs tend to have higher cloud fractions over land, leading to lower surface temperatures that inhibit BB propagation inland (Figs. 12 and 14). Although the land surface boundary conditions are the same across all EMs, the flux contribution is sensitive to the PBL scheme, as seen in Fig. 13, and these verification datasets are sparsely available.

As with any verification study, it is nearly impossible to characterize parameterization errors across four-dimensional space using observations. Looking forward, the TRACER ARM Mobile Facility (AMF) site had the greatest density of observations during the campaign, including flux stations, PBL profilers, and radiosonde releases, which could be used to expand the analysis. This location was not selected as our focus due to the inability to dissect the BB from the SB, but it offers more interactions between the SB and urban land use. Additionally, the extensive data assimilation that creates a more realistic base state for WoFS also complicates quantifying and separating these errors from parameterization. Even though there are inherent differences due to the initial condition perturbation, there is still coherence that can be found across parameterization combinations, providing an avenue to perform analyses across wider time scales.

Although this is a single case, it holds value in understanding how parameterization combinations vary and how those differences can influence air quality or weather forecasts. The impact of the SW radiation scheme on the PBL has been evaluated less often, but it is important for local schemes as they are slower to adjust the PBL. Across all PBL schemes, the RRTMG scheme EMs have better SB timing and larger land–bay temperature gradients. The YSU EMs have the best kinematic representation of the PBL but are too warm and dry, consistent with previous literature (Hu et al. 2010; Milovac et al. 2016). For Houston–Galveston air quality research, it is important to simulate the BB, for which YSU EMs have the most success. However, they produce the deepest PBLs, similar to Salvador et al. (2016), which dilutes pollutants. There is no perfect parameterization combination, but configurations can be optimized based on simulation priorities.

Acknowledgments. This work was supported by the U.S. Department of Energy (DE-SC0021381 and DE-SC0021194).

We would like to acknowledge the support of the University of Houston for access to conduct flight operations.

Data availability statement. All data from the CLAMPS and SPARC systems are postprocessed and quality controlled prior to use for research purposes and can be found on the ARM Data Discovery TRACER catalog (https://doi.org/10.5439/1975084). TRACER-UAS CopterSonde data are available through the ARM data center (https://doi.org/10.5439/1969004). WoFS simulation data are available upon request.

REFERENCES

Arrillaga, J. A., C. Yagüe, M. Sastre, and C. Román-Cascón, 2016: A characterisation of sea-breeze events in the eastern Cantabrian coast (Spain) from observational data and WRF simulations. *Atmos. Res.*, **181**, 265–280, https://doi.org/10.1016/j.atmosres.2016.06.021.

——, J. V.-G. de Arellano, F. Bosveld, H. K. Baltink, C. Yagüe, M. Sastre, and C. Román-Cascón, 2018: Impacts of afternoon and evening sea-breeze fronts on local turbulence, and on CO_2 and radon-222 transport. *Quart. J. Roy. Meteor. Soc.*, **144**, 990–1011, https://doi.org/10.1002/qj.3252.

——, P. Jiménez, J. V.-G. de Arellano, M. A. Jiménez, C. Román-Cascón, M. Sastre, and C. Yagüe, 2020: Analyzing the synoptic-, meso- and local- scale involved in sea breeze formation and frontal characteristics. *J. Geophys. Res. Atmos.*, **125**, e2019JD031302, https://doi.org/10.1029/2019JD031302.

Azorin-Molina, C., S. Tijm, E. E. Ebert, S.-M. Vicente-Serrano, and M.-J. Estrela, 2015: High resolution HIRLAM simulations of the role of low-level sea-breeze convergence in initiating deep moist convection in the eastern Iberian Peninsula. *Bound.-Layer Meteor.*, **154**, 81–100, https://doi.org/10.1007/s10546-014-9961-z.

Baker, R. D., B. H. Lynn, A. Boone, W.-K. Tao, and J. Simpson, 2001: The influence of soil moisture, coastline curvature, and land-breeze circulations on sea-breeze-initiated precipitation. *J. Hydrometeor.*, **2**, 193–211, https://doi.org/10.1175/1525-7541(2001)002<0193:TIOSMC>2.0.CO;2.

Banta, R. M., and Coauthors, 2005: A bad air day in Houston. *Bull. Amer. Meteor. Soc.*, **86**, 657–670, https://doi.org/10.1175/BAMS-86-5-657.

Boybeyi, Z., and S. Raman, 1992: A three-dimensional numerical sensitivity study of convection over the Florida Peninsula. *Bound.-Layer Meteor.*, **60**, 325–359, https://doi.org/10.1007/BF00155201.

Boyer, C. H., J. M. Keeler, and B. C. Rakoczy, 2025: An idealized parameter study of destabilization and convection initiation in coastal regions. Part I: Calm or offshore synoptic-scale flow. *J. Atmos. Sci.*, **82**, 519–539, https://doi.org/10.1175/JAS-D-23-0180.1.

Caicedo, V., and Coauthors, 2019: Bay breeze and sea breeze circulation impacts on the planetary boundary layer and air quality from an observed and modeled DISCOVER-AQ Texas case study. *J. Geophys. Res. Atmos.*, **124**, 7359–7378, https://doi.org/10.1029/2019JD030523.

Cana, L., D. Grisolía-Santos, and A. Hernández-Guerra, 2020: A numerical study of a sea breeze at Fuerteventura Island, Canary Islands, Spain. *Bound.-Layer Meteor.*, **175**, 277–296, https://doi.org/10.1007/s10546-020-00506-z.

Challa, V. S., and Coauthors, 2009: A simulation study of mesoscale coastal circulations in Mississippi Gulf coast. *Atmos. Res.*, **91**, 9–25, https://doi.org/10.1016/j.atmosres.2008.05.004.

Chen, G., H. Iwai, S. Ishii, K. Saito, H. Seko, W. Sha, and T. Iwasaki, 2019: Structures of the sea-breeze front in dual-Doppler lidar observation and coupled mesoscale-to-LES modeling. *J. Geophys. Res. Atmos.*, **124**, 2397–2413, https://doi.org/10.1029/2018JD029017.

Cohen, A. E., S. M. Cavallo, M. C. Coniglio, and H. E. Brooks, 2015: A review of planetary boundary layer parameterization schemes and their sensitivity in simulating southeastern U.S. cold season severe weather environments. *Wea. Forecasting*, **30**, 591–612, https://doi.org/10.1175/WAF-D-14-00105.1.

Colby, F. P., Jr., 2004: Simulation of the New England sea breeze: The effect of grid spacing. *Wea. Forecasting*, **19**, 277–285, https://doi.org/10.1175/1520-0434(2004)019<0277:SOTNES>2.0.CO;2.

Coniglio, M. C., J. Correia Jr., P. T. Marsh, and F. Kong, 2013: Verification of convection-allowing WRF Model forecasts of the planetary boundary layer using sounding observations. *Wea. Forecasting*, **28**, 842–862, https://doi.org/10.1175/WAF-D-12-00103.1.

Crosman, E. T., and J. D. Horel, 2010: Sea and lake breezes: A review of numerical studies. *Bound.-Layer Meteor.*, **137**, 1–29, https://doi.org/10.1007/s10546-010-9517-9.

Cuchiara, G. C., and Coauthors, 2023: Effect of marine and land convection on wet scavenging of ozone precursors observed during a SEAC^{4}RS case study. *J. Geophys. Res. Atmos.*, **128**, e2022JD037107, https://doi.org/10.1029/2022JD037107.

Darby, L. S., 2005: Cluster analysis of surface winds in Houston, Texas, and the impact of wind patterns on ozone. *J. Appl. Meteor.*, **44**, 1788–1806, https://doi.org/10.1175/JAM2320.1.

Dowell, D. C., and Coauthors, 2022: The High-Resolution Rapid Refresh (HRRR): An hourly updating convection-allowing forecast model. Part I: Motivation and system description. *Wea. Forecasting*, **37**, 1371–1395, https://doi.org/10.1175/WAF-D-21-0151.1.

Dudhia, J., 1989: Numerical study of convection observed during the winter monsoon experiment using a mesoscale two-dimensional model. *J. Atmos. Sci.*, **46**, 3077–3107, https://doi.org/10.1175/1520-0469(1989)046<3077:nsocod>2.0.co;2.

Garratt, J. R., and W. L. Physick, 1985: The inland boundary layer at low latitudes: II sea-breeze influences. *Bound.-Layer Meteor.*, **33**, 209–231, https://doi.org/10.1007/BF00052056.

Gómez, I., R. J. Ronda, V. Caselles, and M. J. Estrela, 2016: Implementation of non-local boundary layer schemes in the regional atmospheric modeling system and its impact on simulated mesoscale circulations. *Atmos. Res.*, **180**, 24–41, https://doi.org/10.1016/j.atmosres.2016.04.020.

He, J., D. Chen, Y. Gu, H. Jia, K. Zhong, and Y. Kang, 2022: Evaluation of planetary boundary layer schemes in WRF model for simulating sea-land breeze in Shanghai, China. *Atmos. Res.*, **278**, 106337, https://doi.org/10.1016/j.atmosres.2022.106337.

Heinselman, P. L., and Coauthors, 2024: Warn-on-Forecast System: From vision to reality. *Wea. Forecasting*, **39**, 75–95, https://doi.org/10.1175/WAF-D-23-0147.1.

Hock, N., F. Zhang, and Z. Pu, 2022: Numerical simulations of a Florida sea breeze and its interactions with associated convection: Effects of geophysical representation and model resolution. *Adv. Atmos. Sci.*, **39**, 697–713, https://doi.org/10.1007/s00376-021-1216-6.

Hong, S.-Y., Y. Noh, and J. Dudhia, 2006: A new vertical diffusion package with an explicit treatment of entrainment processes. *Mon. Wea. Rev.*, **134**, 2318–2341, https://doi.org/10.1175/MWR3199.1.

Hu, X.-M., J. W. Nielsen-Gammon, and F. Zhang, 2010: Evaluation of three planetary boundary layer schemes in the WRF model. *J. Appl. Meteor. Climatol.*, **49**, 1831–1844, https://doi.org/10.1175/2010JAMC2432.1.

Huang, H.-Y., A. Hall, and J. Teixeira, 2013: Evaluation of the WRF PBL parameterizations for marine boundary layer clouds: Cumulus and stratocumulus. *Mon. Wea. Rev.*, **141**, 2265–2271, https://doi.org/10.1175/MWR-D-12-00292.1.

Iacono, M. J., J. S. Delamere, E. J. Mlawer, M. W. Shephard, S. A. Clough, and W. D. Collins, 2008: Radiative forcing by long-lived greenhouse gases: Calculations with the AER radiative transfer models. *J. Geophys. Res.*, **113**, D13103, https://doi.org/10.1029/2008JD009944.

Janjić, Z. I., 1994: The step-mountain eta coordinate model: Further developments of the convection, viscous sublayer, and turbulence closure schemes. *Mon. Wea. Rev.*, **122**, 927–945, https://doi.org/10.1175/1520-0493(1994)122<0927:tsmecm>2.0.co;2.

Jensen, M. P., and Coauthors, 2022: A succession of cloud, precipitation, aerosol, and air quality field experiments in the coastal urban environment. *Bull. Amer. Meteor. Soc.*, **103**, 103–105, https://doi.org/10.1175/BAMS-D-21-0104.1.

Jia, W., and Coauthors, 2023: Comprehensive evaluation of typical planetary boundary layer (PBL) parameterization schemes in China—Part 2: Influence of uncertainty factors. *Geosci. Model Dev.*, **16**, 6833–6856, https://doi.org/10.5194/gmd-16-6833-2023.

Lappin, F., and Coauthors, 2024: Data collected using small uncrewed aircraft systems during the TRacking Aerosol Convection interactions ExpeRiment (TRACER). *Earth Syst. Sci. Data*, **16**, 2525–2541, https://doi.org/10.5194/essd-16-2525-2024.

——, T. Bell, P. Klein, and G. de Boer, 2025: Quantifying the thermodynamic impacts on the atmospheric boundary layer due to the sea breeze in the coastal Houston region. *J. Appl. Meteor. Climatol.*, **64**, 607–623, https://doi.org/10.1175/JAMC-D-24-0203.1.

LeMone, M. A., M. Tewari, F. Chen, and J. Dudhia, 2013: Objectively determined fair-weather CBL depths in the ARW-WRF Model and their comparison to CASES-97 observations. *Mon. Wea. Rev.*, **141**, 30–54, https://doi.org/10.1175/MWR-D-12-00106.1.

Li, W., Y. Wang, C. Bernier, and M. Estes, 2020: Identification of sea breeze recirculation and its effects on ozone in Houston, TX, during DISCOVER-AQ 2013. *J. Geophys. Res. Atmos.*, **125**, e2020JD033165, https://doi.org/10.1029/2020JD033165.

Mansell, E. R., C. L. Ziegler, and E. C. Bruning, 2010: Simulated electrification of a small thunderstorm with two-moment bulk microphysics. *J. Atmos. Sci.*, **67**, 171–194, https://doi.org/10.1175/2009JAS2965.1.

Melas, D., and H. D. Kambezidis, 1992: The depth of the internal boundary layer over an urban area under sea-breeze conditions. *Bound.-Layer Meteor.*, **61**, 247–264, https://doi.org/10.1007/BF02042934.

Miao, J.-F., K. Wyser, D. Chen, and H. Ritchie, 2009: Impacts of boundary layer turbulence and land surface process parameterizations on simulated sea breeze characteristics. *Ann. Geophys.*, **27**, 2303–2320, https://doi.org/10.5194/angeo-27-2303-2009.

Milovac, J., K. Warrach-Sagi, A. Behrendt, F. Späth, J. Ingwersen, and V. Wulfmeyer, 2016: Investigation of PBL schemes combining the WRF model simulations with scanning water vapor differential absorption lidar measurements. *J. Geophys. Res. Atmos.*, **121**, 624–649, https://doi.org/10.1002/2015JD023927.

Montornès Torrecillas, A., 2017: A study of the shortwave schemes in the Weather Research and Forecasting model. Ph.D. Thesis, Universitat de Barcelona, 27 pp., https://hdl.handle.net/10803/401501.

Nakanishi, M., and H. Niino, 2006: An improved Mellor–Yamada Level-3 model: Its numerical stability and application to a regional prediction of advection fog. *Bound.-Layer Meteor.*, **119**, 397–407, https://doi.org/10.1007/s10546-005-9030-8.

Palomaki, R. T., N. T. Rose, M. van den Bossche, T. J. Sherman, and S. F. De Wekker, 2017: Wind estimation in the lower atmosphere using multirotor aircraft. *J. Atmos. Oceanic Technol.*, **34**, 1183–1191, https://doi.org/10.1175/JTECH-D-16-0177.1.

Päschke, E., R. Leinweber, and V. Lehmann, 2015: An assessment of the performance of a 1.5 μm Doppler lidar for operational vertical wind profiling based on a 1-year trial. *Atmos. Meas. Tech.*, **8**, 2251–2266, https://doi.org/10.5194/amt-8-2251-2015.

Potvin, C. K., and Coauthors, 2020: Assessing systematic impacts of PBL schemes on storm evolution in the NOAA Warn-on-Forecast System. *Mon. Wea. Rev.*, **148**, 2567–2590, https://doi.org/10.1175/MWR-D-19-0389.1.

Ryerson, T. B., and Coauthors, 2003: Effect of petrochemical industrial emissions of reactive alkenes and NO*x* on tropospheric ozone formation in Houston, Texas. *J. Geophys. Res.*, **108**, 4249, https://doi.org/10.1029/2002JD003070.

Salvador, N., and Coauthors, 2016: Evaluation of weather research and forecasting model parameterizations under sea-breeze conditions in a North Sea coastal environment. *J. Meteor. Res.*, **30**, 998–1018, https://doi.org/10.1007/s13351-016-6019-9.

Sawyer, V., and Z. Li, 2013: Detection, variations and intercomparison of the planetary boundary layer depth from radiosonde, lidar and infrared spectrometer. *Atmos. Environ.*, **79**, 518–528, https://doi.org/10.1016/j.atmosenv.2013.07.019.

Segales, A. R., B. R. Greene, T. M. Bell, W. Doyle, J. J. Martin, E. A. Pillar-Little, and P. B. Chilson, 2020: The CopterSonde: An insight into the development of a smart unmanned aircraft system for atmospheric boundary layer research. *Atmos. Meas. Tech.*, **13**, 2833–2848, https://doi.org/10.5194/amt-13-2833-2020.

Seidel, D. J., C. O. Ao, and K. Li, 2010: Estimating climatological planetary boundary layer heights from radiosonde observations: Comparison of methods and uncertainty analysis. *J. Geophys. Res.*, **115**, D16113, https://doi.org/10.1029/2009JD013680.

Shin, H. H., and S.-Y. Hong, 2011: Intercomparison of planetary boundary-layer parametrizations in the WRF model for a single day from CASES-99. *Bound.-Layer Meteor.*, **139**, 261–281, https://doi.org/10.1007/s10546-010-9583-z.

Smirnova, T. G., J. M. Brown, S. G. Benjamin, and J. S. Kenyon, 2016: Modifications to the Rapid Update Cycle land surface model (RUC LSM) available in the Weather Research and Forecasting (WRF) Model. *Mon. Wea. Rev.*, **144**, 1851–1865, https://doi.org/10.1175/MWR-D-15-0198.1.

Stanier, C. O., and Coauthors, 2021: Overview of the Lake Michigan Ozone Study 2017. *Bull. Amer. Meteor. Soc.*, **102**, E2207–E2225, https://doi.org/10.1175/BAMS-D-20-0061.1.

Stensrud, D. J., 2007: *Parameterization Schemes: Keys to Understanding Numerical Weather Prediction Models.* Cambridge University Press, 459 pp.

——, and Coauthors, 2009: Convective-scale warn-on-forecast system: A vision for 2020. *Bull. Amer. Meteor. Soc.*, **90**, 1487–1500, https://doi.org/10.1175/2009BAMS2795.1.

Stoll, R., J. A. Gibbs, S. T. Salesky, W. Anderson, and M. Calaf, 2020: Large-eddy simulation of the atmospheric boundary layer. *Bound.-Layer Meteor.*, **177**, 541–581, https://doi.org/10.1007/s10546-020-00556-3.

Stull, R. B., 2012: *An Introduction to Boundary Layer Meteorology.* Vol. 13. Springer Science and Business Media, 670 pp.

Turner, D. D., and W. G. Blumberg, 2019: Improvements to the AERIoe thermodynamic profile retrieval algorithm. *IEEE J. Sel. Top. Appl. Earth Obs. Remote Sens.*, **12**, 1339–1354, https://doi.org/10.1109/JSTARS.2018.2874968.

Wagner, T. J., P. M. Klein, and D. D. Turner, 2019: A new generation of ground-based mobile platforms for active and passive profiling of the boundary layer. *Bull. Amer. Meteor. Soc.*, **100**, 137–153, https://doi.org/10.1175/BAMS-D-17-0165.1.

Wang, D., E. C. Melvin, N. Smith, M. P. Jensen, S. Gupta, A. Abdullah-Smoot, N. Pszeniczny, and T. Hahn, 2024: TRACER perspectives on gulf-breeze and bay-breeze circulations and coastal convection. *Mon. Wea. Rev.*, **152**, 2207–2228, https://doi.org/10.1175/MWR-D-23-0292.1.

Xie, B., J. C. H. Fung, A. Chan, and A. Lau, 2012: Evaluation of nonlocal and local planetary boundary layer schemes in the WRF model. *J. Geophys. Res.*, **117**, D12103, https://doi.org/10.1029/2011JD017080.

Zhang, L., and Coauthors, 2022: Adaptability evaluation of boundary layer schemes for simulation of sea and land breeze circulation in the west coast of the Yellow Sea. *Atmos. Res.*, **278**, 106354, https://doi.org/10.1016/j.atmosres.2022.106354.

Zhong, S., H. In, and C. Clements, 2007: Impact of turbulence, land surface, and radiation parameterizations on simulated boundary layer properties in a coastal environment. *J. Geophys. Res.*, **112**, D13110, https://doi.org/10.1029/2006JD008274.

Zhou, X., and Coauthors, 2022: The development of the NCEP Global Ensemble Forecast System version 12. *Wea. Forecasting*, **37**, 1069–1084, https://doi.org/10.1175/WAF-D-21-0112.1.